Integrating immune library probing with structure-based computational design to develop potent neutralizing nanobodies against emerging SARS-CoV-2 variants

Lidia Cerdán, Katixa Silva, Daniel Rodríguez-Martín, Patricia Pérez, María A. Noriega, Ana Esteban Martín, Alfonso Gutiérrez-Adán, Yago Margolles, Juan A. Corbera, Miguel A. Martín-Acebes, Juan García-Arriaza, Juan Fernández-Recio, Luis A. Fernández & José M. Casasnovas

View supplementary material

Published online: 06 May 2025.

Submit your article to this journal

Article views: 538

View related articles

View Crossmark data

Taylor & Francis
Taylor & Francis Group

REPORT

🔓 OPEN ACCESS | Check for updates

Integrating immune library probing with structure-based computational design to develop potent neutralizing nanobodies against emerging SARS-CoV-2 variants

Lidia Cerdán [ID][a], Katixa Silva[b], Daniel Rodríguez-Martín [ID][c], Patricia Pérez [ID][c,d], María A. Noriega[b,c], Ana Esteban Martín[e], Alfonso Gutiérrez-Adán[f], Yago Margolles [ID][a], Juan A. Corbera[g], Miguel A. Martín-Acebes[e], Juan García-Arriaza [ID][c,d], Juan Fernández-Recio [ID][h], Luis A. Fernández [ID][a], and José M. Casasnovas [ID][b]

aDepartment of Microbial Biotechnology, Consejo Superior de Investigaciones Científicas (CNB-CSIC), Madrid, Spain; bDepartment of Macromolecular Structures, Consejo Superior de Investigaciones Científicas (CNB-CSIC), Madrid, Spain; cDepartment of Molecular and Cellular Biology, Centro Nacional de Biotecnología, Consejo Superior de Investigaciones Científicas (CNB-CSIC), Madrid, Spain; dCentro de Investigación Biomédica en Red de Enfermedades Infecciosas (CIBERINFEC), Madrid, Spain; eDepartment of Biotechnology, Instituto Nacional de Investigación y Tecnología Agraria y Alimentaria, Consejo Superior de Investigaciones Científicas (INIA-CSIC), Madrid, Spain; fDepartment of Animal Reproduction, INIA-CSIC, Madrid, Spain; gInstituto Universitario de Investigaciones Biomédicas y Sanitarias (IUIBS), Facultad de Veterinaria, Universidad de Las Palmas de Gran Canaria (ULPGC), Campus Universitario de Arucas, Gran Canaria, Spain; hInstituto de Ciencias de la Vid y del Vino (ICVV), CSIC - Universidad de La Rioja - Gobierno de La Rioja, Logroño, Spain

ABSTRACT

To generate antibodies (Abs) against SARS-CoV-2 emerging variants, we integrated multiple tools and engineered molecules with excellent neutralizing breadth and potency. Initially, the screening of an immune library identified a nanobody (Nb), termed Nb4, specific to the receptor-binding domain (RBD) of the Omicron BA.1 variant. A Nb4-derived heavy chain antibody (hcAb4) recognized the spike (S) of the Wuhan, Beta, Delta, Omicron BA.1, and BA.5 SARS-CoV-2 variants. A high-resolution crystal structure of the Nb4 variable (VHH) domain in complex with the SARS-CoV-2 RBD (Wuhan) defined the Nb4 binding mode and interface. The Nb4 VHH domain grasped the RBD and covered most of its outer face, including the core and the receptor-binding motif (RBM), which was consistent with hcAb4 blocking RBD binding to the SARS-CoV-2 receptor. In mouse models, a humanized hcAb4 showed therapeutic potential and prevented the replication of SARS-CoV-2 BA.1 virus in the lungs of the animals. *In vitro*, hcAb4 neutralized Wuhan, Beta, Delta, Omicron BA.1, and BA.5 viral variants, as well as the BQ.1.1 subvariant, but showed poor neutralization against the Omicron XBB.1.5. Structure-based computation of the RBD–Nb4 interface identified three Nb4 residues with a reduced contribution to the interaction with the XBB.1.5 RBD. Site-saturation mutagenesis of these residues resulted in two hcAb4 mutants with enhanced XBB.1.5 S binding and virus neutralization, further improved by mutant Nb4 trimers. This research highlights an approach that combines library screening, Nb engineering, and structure-based computational predictions for the generation of SARS-CoV-2 Omicron-specific Abs and their adaptation to emerging variants.

Introduction

Circulation of severe acute respiratory syndrome coronavirus 2 (SARS-CoV-2) among the human population has resulted in the emergence of numerous viral variants with enhanced transmission and escape from neutralizing antibodies (Abs).[1–4] These variants have accumulated mutations in the envelope spike (S) glycoprotein and its receptor-binding domain (RBD),[1] which is the main target of neutralizing Abs in coronavirus.[1,5,6] Numerous Abs and nanobodies (Nbs) recognizing the SARS-CoV-2 RBD have been identified and clustered based on the RBD regions and/or conformations recognized.[6–9] Class I or II Abs bind to the receptor-binding motif (RBM), but class I Abs recognize only the open RBD conformation.[7] Class III and IV Abs recognize the outer and inner sides of the RBD, respectively. In addition, class V Abs recognize the RBD front, which is hidden in the closed conformation.[10,11]

Since the emergence of the original Wuhan strain, SARS-CoV-2 has accumulated mutations in the S,[12] particularly in the Omicron variant that emerged in South Africa in late 2021 and acquired 30 amino acid substitutions in the S, half of them in the RBD.[13] These mutations increased the reproductive number of the virus and boosted the transmission of the first Omicron BA.1 lineage, which replaced the Delta variant worldwide. Even though the Alpha, Beta, and Delta variants bear one to three key substitutions in the RBD that affect the neutralizing potency of some Abs, the emergence of the Omicron variants with more than 15 RBD mutations in and out of the RBM raised serious concerns about the efficacy of

vaccines and neutralizing Abs.[14–16] The Omicron BA.2 lineage displaced BA.1 and evolved into two major sublineages, the BA.4/BA.5 and the XBB, which accumulated up to nine additional mutations in the RBD of the XBB.1.16 subvariant with respect to BA.2. The acquisition of the P486 residue in the XBB.1.5 subvariant increased its affinity for angiotensin converting enzyme 2 (ACE2) and favored its transmission and global expansion.[14] The XBB sublineage exhibits an extraordinary ability to evade vaccine-induced Ab neutralization, and among the approved commercial Abs, only sotrovimab has some neutralizing activity.[14,17] Unlike the BA.2 or XBB variants, the BA.4/BA.5 sublineage contains the L452R mutation also found in the Delta variant, which is known to increase ACE2 binding affinity. The Omicron BQ.1.1 subvariant evolved from the BA.5 by the acquisition of several mutations (K444T, N460K, and R346T) that favored Ab evasion and its spread in many countries due to its higher ACE2 binding affinity than the XBB.1 subvariant, although lower than XBB.1.5.[12] The sera from vaccinated or infected individuals show much lower neutralization titers for the BQ and XBB subvariants than for the original BA.5 and BA.2, respectively, and most of the BA.5 and BA.2 neutralizing Abs failed to neutralize the BQ and XBB viruses.[18] This phenomenon is attributed to the antigenic drift of these subvariants, which became more distant from the original SARS-CoV-2, SARS-CoV-1, or other animal sarbecoviruses.

Despite the continuous accumulation of mutations in the S and RBD of the SARS-CoV-2 Omicron variants, vaccines remained effective in preventing severe COVID-19 and hospitalization in the large majority of the human population.[19,20] Nonetheless, the approved therapeutic Abs for use in SARS-CoV-2-infected and hospitalized patients failed to efficiently neutralize the most evolved viral variants.[18] Screening of Ab libraries generated from immunized or infected individuals with selected viral antigens can be used to identify Abs that neutralize multiple SARS-CoV-2 variants or even different sarbecoviruses.[21–23] Similarly, Nbs with broad neutralization can be found in libraries prepared from immunized camelids[24–27] or from synthetic libraries.[28,29] Alternatively, computational methods are being used to model or redesign Abs or Nbs and tailor them to specific variants.[28,30–33] Some of these approaches generate or evolve Nbs by applying docking methods to predict potential affinity-enhancing mutations,[31] or machine learning and molecular dynamics (MD) to predict the effect of mutations on binding affinity[32]; others rely specifically on complementarity-determining regions (CDRs) designed from random sequence libraries[28] or by structure-guided high-throughput in silico mutagenesis of CDRs, protein–protein docking for screening, and MD simulations for stability.[33] In addition, multivalent or multispecific Ab-based molecules are being designed to counteract SARS-CoV-2 evolution.[29,34–36]

Previously, we generated a Nb immune library from two dromedaries immunized with the RBD of the Wuhan variant and identified RBD-specific Nbs that recognized and neutralized SARS-CoV-2 variants other than Omicron.[37] As reported here, we selected a potent and broadly neutralizing Nb (Nb4) from this immune library and generated a heavy chain Ab (hcAb4) and multimeric Nb4 molecules that efficiently neutralized the Wuhan, Beta, Delta, Omicron BA.1, BA.5, and BQ.1.1 variants

and significantly reduced the viral load in K18-hACE2 transgenic mice infected with SARS-CoV-2 BA.1. In addition, based on the crystal structure of the RBD–Nb4 complex, we applied a computational and mutagenesis procedure directed toward key contacts in the binding interface to enhance the Nb4 neutralization of Omicron XBB subvariants. This unique approach combines library screening and Nb engineering with structure- and computation-based Ab evolution and could be widely applied for Ab adaptation to emerging viral variants.

Materials and methods

Methods for Nb selection from an immune library displayed in bacteria, recombinant DNA preparation and expression of hcAb, S, and RBD proteins in mammalian cells and the procedures followed for enzyme-linked immunosorbent assays (ELISA) to evaluate protein–protein interactions have been reported previously,[37] and they are further described in supplemental online materials. The remaining methods are described below.

Expression of Nb4 and ACE2 in Pichia pastoris and purification

The cDNA encoding the Nb4 was amplified by polymerase chain reaction (PCR), digested with XhoI and SalI, and cloned into the corresponding sites in the *pPICzαA* vector, in frame with the *alpha*-factor at the 5' end and a His-tag at the 3' end. To express trimeric Nb4 molecules (Nb4 × 3), we cloned a second and a third Nb4 sequence in tandem at the unique SalI site, after cDNA amplification with a 5' primer with a sequence coding for the (GGGGS)x3 linker. The *pPICzαA*/Nb4 and *pPICzαA*/Nb4×3 constructs were linearized with SacI and transformed into the yeast strain BG11 by electroporation, and clones were selected in yeast extract peptone dextrose (YPD) agar plates supplemented with 100 μg/ml of zeocin following recommended procedures (Invitrogen). Yeast clones producing Nb4 or Nb4 × 3 were grown (500 ml) in buffered glycerol-complex medium (BMGY), and after 24 h, the cells were sedimented and resuspended in 250 ml of buffered methanol-complex medium (BMMY) medium for induction of the protein expression with methanol during 72 h. The Nb4 proteins were purified from the cell culture with a Nickel Agarose Extrachel™ (ABT) column, and the eluted protein with 250 mM imidazole in Tris-buffer saline (TBS, 20 mM Tris-HCl, 200 mM NaCl, pH 8.0) was concentrated and run through a Superdex 75 (10/300) column with HEPES-buffer saline (HBS, 20 mM HEPES, 150 mM NaCl, pH 7.5).

hcAb4 competition of the RBD-ACE2 interaction was carried out with unlabeled RBD-Fc and a human ACE2 ectodomain produced in *Pichia pastoris*. A region encoding ACE2 residues 19–615 was cloned into the EcoRI and SalI of the *pPICzαA* vector, in frame with the *alpha*-factor at the 5' end and a His-tag at the 3' end; it was produced in the yeast strain BG11 and purified as described for the Nb4 above. The protein at 10 μg/ml was coated overnight in immunoplates (Maxisorp, Nunc) and binding of the RBD-Fc protein without or with

increasing concentrations of the hcAb4 was analyzed as described in detail previously.[37]

RBD–Nb4 complex crystallization and structure determination

An RBD (Wuhan) with high mannose glycosylation was prepared by stable expression in Chinese hamster ovary (CHO) Lec.3.8.2.1 cells as previously described.[38] The RBD containing residues 332–534 of the S was produced fused to the HA-tag and the IgG1 Fc portion at the N and C-terminal ends, respectively, and it was prepared and purified free of tags as reported.[39] The RBD was endoglycosidase H-treated overnight at 30ºC to remove the N-linked glycans prior to size exclusion chromatography (SEC) purification in TBS.

To crystallize the complex, the deglycosylated RBD and the Nb4 proteins in TBS were mixed in a molar ratio 1:1.1 and incubated overnight at 4ºC prior to crystallization trials using the JCSG + + and Pi-minimal kits (Jena Bioscience). The protein complex crystallized by the sitting drop method with several crystallization conditions, although the best diffraction dataset at 1.21 Å resolution (Table 1) was collected from a crystal prepared with 22.5% PEG 8000, 200 mM NaCl and 100 mM NaAc pH 4.5, which was flash-frozen in the same solution with 20% ethylene glycol. Crystal structure of the complex was determined by the molecular replacement method using structures of the RBD (PDB ID 6YLA) and a Nb (PDB ID 6H71) with the program PHASER[40]; the model was manually adjusted to the electron density in COOT[41] and refined with

Table 1. Data collection and refinement statistics.

	RBD–Nb4: PDB ID 9FC2
Data Processing	
Space group	P61
Cell dimensions	
a, b, c (Å)	97.66 97.66 64.35
α, β, γ(°)	90 90 120
Wavelength	0.97926 Å
Resolution (Å)	48.83–1.21 (1.23–1.21)
Unique reflections	103166 (3501)
Redundancy	9.9 (8.3)
Completeness (%)	97.2 (100)
I/σ(I)	22.24 (2.1)
R-merge	4.4 (81.4)
R-pin	1.5 (30.0)
CC1/2	99.96 (82.34)
Refinement	
Resolution (Å)	48.83–1.21 (1.22–1.21)
R-work	15.27 (21.88)
R-free	16.99 (25.36)
Non-hydrogen atoms	2965
Protein	2575
Ligands	26
Solvent	364
Average B-factors	23.7
Protein	22.3
Ligands	43.0
Solvent	32.1
R.m.s deviations	
Bond lengths (Å)	0.014
Bond angles (°)	1.23
Ramachandran plot	98/2/0/0

Statistics for the highest resolution shell are in parentheses. Residues (%) in the most favored/allowed/generously allowed/disfavored regions of the Ramachandran plot are shown.

PHENIX.[42] The refinement statistics are shown in Table 1 and the electron density map is presented in Figure S1. The RBD-Nb binding interface was determined with the PISA server, and the figures of the structure were prepared with pymol (pymol.org). Coordinates and structure factors have been deposited in the Protein Data Bank with ID code 9FC2.

Binding kinetics and affinity determination

We applied surface plasmon resonance in a BIAcore 3000 instrument (GE Healthcare) to determine the Nb4/hcAb4 binding to the RBD protein. RBD-Fc (~ 1000RU) or RBD-FH (~ 500RU) proteins were immobilized in different flow cells of CM5 chips. Subsequently, several concentrations of Nb4 or hcAb4 in HBS buffer were injected at 30 μl/min through sensor chip surfaces with and without RBD during 4 min. After 4 min. of dissociation phase, the surfaces were regenerated with two injection of 10 mM glycine pH 1.7. The binding kinetics were determined by the analysis of the sensorgrams with the BIAEvaluation 3.0 software after double correction of the signal with that of the empty flow cell surface and with a sensorgram recorded for buffer injection through the surface with RBD. Separate and simultaneous fitting or association and dissociation phases were applied and the resulting kinetics averaged.

In vitro neutralization of live SARS-CoV-2

Several SARS-CoV-2 strains were used to evaluate *in vitro* virus neutralization: The SARS-CoV-2 isolate MAD6, similar to the Wuhan strain but carrying the D614G mutation in the S protein, was kindly provided by Prof Luis Enjuanes (CNB-CSIC, Madrid, Spain); the SARS-CoV-2 Beta (B.1.351) variant (hCoV-19/France/PDL-IPP01065i /2021) isolated by Dr J. Besson (Bioliance Laboratory, Saint-Herblain; France) was supplied by the European Virus Archive-Global (EVAG); the SARS-CoV-2 Delta (B.1.617) variant (SARS-CoV-2, Human, 2021, Germany ex India, 20A/452 R) isolated by Dr Andreas Nitsche (Robert Koch Institute, Berlin, Germany) was also acquired from the EVAG; the SARS-CoV-2 BA.1 (B.1.1.529) Omicron variant (hCoV-19/Belgium/rega -20,174/2021, EPI_ISL_6794907) was supplied by Prof Piet Maes from KU Leuven (Belgium); the SARS-CoV-2 Omicron BA.5 (EPI_ISL_13424827), BQ.1.1 (EPI_ISL_15653663), XBB.1.5 (EPI_ISL_16939528), and XBB.1.16 (EPI_ISL_17535655) subvariants were provided by Prof Rafael Delgado (Hospital Universitario 12 de Octubre, Madrid, Spain). The infectivity titers of the SARS-CoV-2 viral stocks resulting from infection of Vero/TMPRSS2 cells were determined by plaque assay or by a median tissue culture infectious dose (TCID$_{50}$) assay in Vero-E6 cells, as previously described.[43] The ability of different recombinant Nbs or Abs to neutralize live SARS-CoV-2 variants of concern (VoCs) was assayed by a microneutralization test (MNT) assay in a BSL-3 laboratory at the CNB-CSIC, as reported,[43] and it is described in supplemental online materials.

In vivo therapeutic efficacy of the hcAb4 in SARS-CoV-2-infected mice

A total of 15 six-week-old hemizygous female K18-hACE2 transgenic mice expressing human ACE2 under the control of the human cytokeratin 18 gene promoter at CISA-INIA-CSIC were used.[44] Mice were anesthetized under isoflurane and inoculated intranasally (in) with 50 μl of Dulbecco's modified eagle medium (DMEM) containing 10^4 TCID$_{50}$ of SARS-CoV-2 Omicron lineage BA.1.17 (hCoV-19/Spain/MD-H12O_1620/2021; Gisaid: EPI_ISL_7781198) kindly provided by Prof Rafael Delgado (Hospital 12 de Octubre, Madrid, Spain). Virus was titrated as TCID$_{50}$/ml using end-point dilutions in 96-well plates. Five mice per group were inoculated intraperitoneally (ip) with 150 μg of each Ab in 150 μl of HBS at 24 h post-infection. Animals received water and food *ad libitum* and they were monitored daily for clinical signs and body weight, anesthetized, and sacrificed by cervical dislocation at 4 days post-infection (dpi). Lungs were harvested and homogenized in RLT lysis buffer (Qiagen) using a TissueLyser II equipment. RNA was extracted using IndiMag Pathogen kit (Indical Bioscience) and an IndiMag 48s automated nucleic acid extractor. The amount of viral genomic RNA was determined as described by quantitative RT-PCR.[44] Data were expressed as TCID$_{50}$ equivalents/g of lung tissue by comparison with previously titrated samples.

Computing RBD–Nb4 binding energies

Binding energy between RBD and Nb4 in the crystal structure of the complex was computed with pyDock *bindEy* module.[45,46] In order to compare later with other modeled variants, all the side chains in the RBD–Nb4 complex structure were minimized with the SCWRL program. Since two versions of this program were available, and it is not clear which one provides better predictive rates based on our previous experience in minimizing protein–protein docking models, we used both the original SCWRL3[47] and the most recent version SCWRL4.[48]

The RBD in the XBB.1.5 subvariant was modeled based on the coordinates in the RBD–Nb4 complex structure, introducing the 22 single mutations relative to the SARS-CoV-2 Wuhan variant by using SCWRL3 or SCWRL4 with the option of minimizing all side chains. The contributions to the binding energy per residue were computed with pyDockEneRes web server (https://life.bsc.es/pid/pydockeneres).[49] This program can also be executed as a module of pyDock software,[45,46] a standalone pipeline for structural and energetic modeling of protein interactions. All potential single residue mutations in Nb4 (120 residues × 19 amino acids) were modeled with *ad-hoc* scripts, using SCWRL4 to build the mutants within the context of the Nb4 in complex with the XBB.1.5 RBD, and pyDock *bindEy* to compute the binding energy for each mutant.

Site-saturation mutagenesis of hcAb4 residues and identification of mutants with high ligand binding activity

To generate hcAb4 mutants, three rounds of mutagenesis for each hcAb4 residue was carried out with primers of 27 nucleotides and having the SNN (5' primer) or NNS (3' primer) triplets for the selected residues, essentially as described by J.D. Bloom[50] and implemented also for deep mutagenesis of SARS-CoV-2 RBD.[51] Each round of mutagenesis following the overlap PCR procedure included three PCR reactions: 7-cycle PCR1 and PCR2 to generate two overlapping DNA fragments with the randomized primers and a third PCR to reconstitute the Nb4 coding cDNAs with the primers CMVF and Nb-C1 contained in the pIg△CH1/Nb4 construct. The final PCR products were cleaved and cloned into the unique ClaI and BamHI of the pIg△CH1 vector and bacterial clones selected in ampicillin plates. Sequencing of several clones confirmed the saturation mutagenesis of the individual Nb4 residues. Subsequently, DNA was prepared for about 80 clones for each mutant and used for transfection of HEK-293T cells using PEImax in 24-well plates with cells in Dulbecco's modified Eagle medium (DMEM) +10% fetal calf serum (FCS). Three days after transfection, the expression of hcAbs in the cell supernatants was monitored by an anti-human Fc sandwich ELISA, and used in binding assays with plastic-bound S proteins as described in supplemental online materials.

Results

Selection of a Nb specific for Omicron RBD from an immune library

Nb4 was identified from an immune library of VHH domains cloned in *Escherichia coli* after immunization of two dromedaries with purified RBD of SARS-CoV-2 Wuhan fused to the Fc region of human IgG1 (RBD-Fc).[37] This VHH library was constructed in the pNeae2 plasmid, enabling display of intimin-Nb fusions on the surface of *E. coli*.[52] We used a population of *E. coli* bacteria from this immune library obtained after magnetic activated cell sorting (MACS) and fluorescence-activated cell sorting (FACS) selections with biotinylated RBD Wuhan.[37] To evaluate whether Nbs specific for a distant SARS-CoV-2 variant could be identified, we further incubated this bacterial population with 100 nM biotinylated RBD-Fc from Omicron BA.1 (RBD-Fc BA.1) as bait in one cycle of FACS (Figure S2a). Flow cytometric analysis of the BA.1-sorted bacteria showed a clear increase in binding to 100 nM of BA.1 RBD-Fc compared to the immune library (Figure S2b), although this population also showed binding to a nonspecific antigen (human fibrinogen) used as a negative control.

Screening by flow cytometry of 30 individual colonies randomly picked from the BA.1-sorted population identified 19 positives that bound to RBD-Fc of BA.1 at 100 nM. DNA sequencing revealed five distinct VHHs, which were named according to their frequencies (indicated in parentheses): Nb1 (12/30), Nb2 (4/30), Nb3 (1/30), Nb4 (1/30), and Nb5 (1/30). Flow cytometric analysis of bacteria clones displaying these Nbs incubated with RBD-Fc BA.1 and control antigens human fibrinogen or PD-L1-Fc revealed that only Nb4 exhibited specific binding to the target antigen RBD-Fc BA.1, while Nb1, Nb2, and Nb3 bound to fibrinogen (Figure S2c), and Nb5 bound to the control Fc protein (PD-L1-Fc) (Figure S2d).

E. coli displaying Nb4 were then further characterized for binding to trimeric S, dimeric RBD-Fc, and monomeric RBD of several SARS-CoV-2 variants, including Omicron BA.1, Omicron BA.5, and the ancestral Wuhan strain. Flow cytometry data indicated that Nb4 binds all these SARS-CoV-2 variants, with significant binding to monomeric RBD of BA.5 and Wuhan at low concentrations (1 nM) (Figure 1). Interestingly, flow cytometry of bacteria displaying Nb4 also showed binding to the dimeric and monomeric RBD of SARS-CoV-1 at a concentration of 100 nM (Figure 1), indicating that Nb4 has potentially broad specificity for different sarbecoviruses.

Production of the Nb4 and a derived heavy chain Ab (hcAb4) and binding to the S or RBD of SARS-CoV-2 variants

To determine the binding properties of the Nb4 for different SARS-CoV-2 S variants, we fused the Nb4 VHH domain to the human IgG1 Fc region and produced the resulting hcAb4 in mammalian cells as described in Materials and methods. In addition, monomeric Nb4 was prepared from the hcAb4 or by

expression in *Pichia pastoris*, which was also used to prepare trimeric Nb4 (Nb4 × 3) containing three VHH domains in tandem joined with a flexible GS-rich linker (see Materials and methods).

The hcAb4 bound to the S of Wuhan, Beta, Delta, Omicron BA.1, and BA.5 with subnanomolar apparent affinities in ELISA (Figure 2a) and prevented RBD binding to ACE2 (Figure 2b), indicating that it could potentially neutralize SARS-CoV-2 by preventing virus entry into host cells. To confirm Nb recognition of the RBD from different variants, we performed RBD-Fc protein binding to monomeric or trimeric Nb4 proteins, which showed identical binding specificity as with S (Figure S3). Consistent with the binding data in bacteria (Figure 1), we observed some interaction of the Nb4 with the SARS-CoV-1 RBD-Fc, mostly with the trimeric Nb4 × 3 (Figure S3). We also determined the kinetics for monomeric Nb4 or hcAb4 binding to Wuhan RBD (Figure 2c). The dissociation rates were quite low and relatively similar for both molecules, suggesting that, despite the dimeric nature of hcAb4, it bound as a monomer to the RBD in this assay. The determined association rates for Nb4/hcAb4 were also
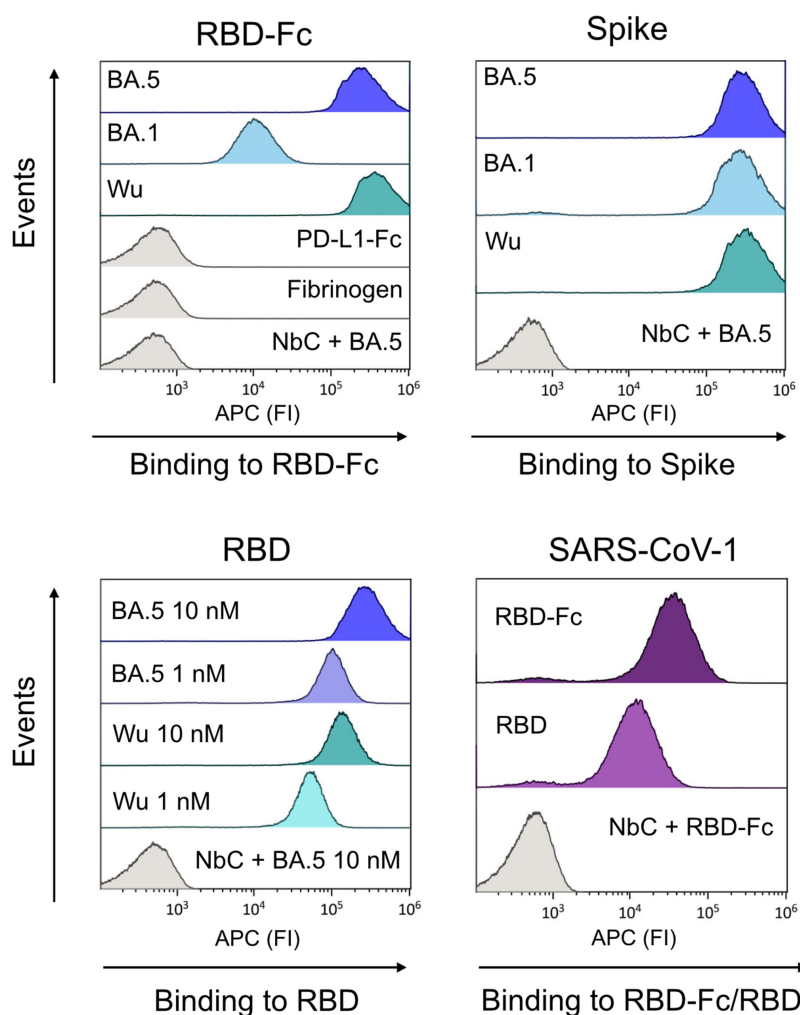

Figure 1. SARS-CoV-2 antigen-binding specificity of selected bacteria expressing Nb4. Flow cytometry of the bacteria with several SARS-CoV-2 Omicron antigens, shown above the panels. A control bacterial clone expressing an unrelated nanobody (NbC) was included. Top left panel: binding to RBD-Fc of BA.5, BA.1, or Wuhan (Wu) and to unrelated antigens PD-L1-Fc and fibrinogen. Top right panel: binding to Spike (S) of BA.5, BA.1, and Wu. Bottom left panel: binding to monomeric RBD of BA.5 and Wu. Bottom right panel: binding to RBD-Fc and monomeric RBD of SARS-CoV-1. Purified proteins were used at 100 nM unless otherwise noted.
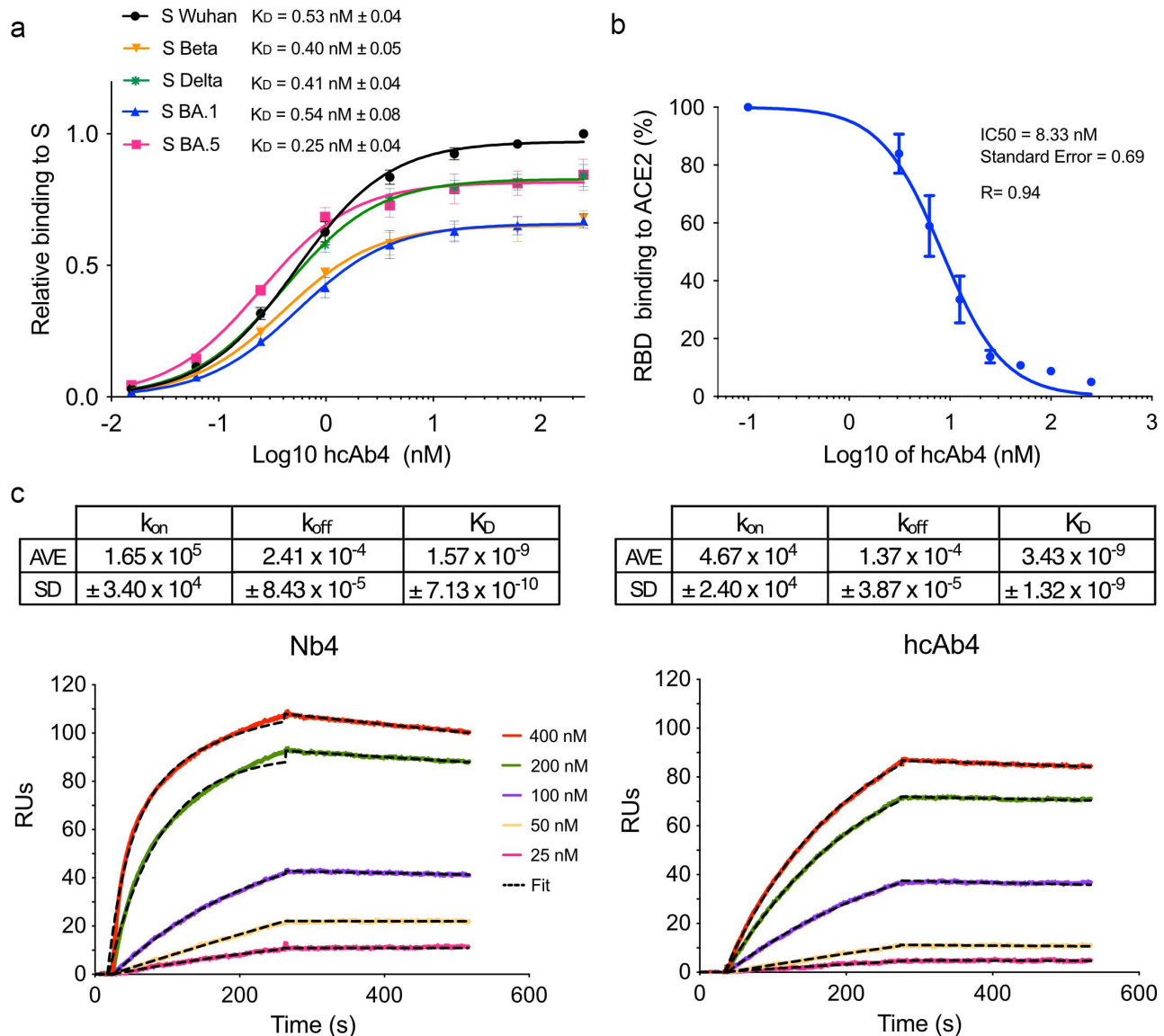
Figure 2. Ligand binding specificity and affinity of the Nb4. (a). Binding of the Nb4-derived hcAb4 to the S of different SARS-CoV-2 variants. Binding of serial ¼ dilutions of the hcAb4 to S variants on plates was carried out as described in supplemental online materials. The binding relative to that determined with the Wuhan S at the highest hcAb4 concentration (250 nM) is shown, as well as the determined apparent K_D values for each S variant. Data were fitted to non-linear regression models using the program GraphPad to determine the apparent K_D. Mean ± standard error of the mean (SEM) from 4–6 independent binding assays. (b). Blocking SARS-CoV-2 RBD binding to its ACE2 receptor by the hcAb4. Binding of the RBD-Fc (Wuhan) to ACE2 in the absence or increasing concentrations of the hcAb4, determined as described in Materials and methods. Mean ± SEM of the binding relative to the sample without hcAb are shown (n = 4). (c). Ligand binding kinetics. Overlayed sensorgrams recorded during the association and dissociation of the monomeric Nb4 (left) or the hcAb4 (right) from RBD (Wuhan) proteins immobilized in a BIAcore sensor chip. Fitting of the corrected sensorgrams to a 1:1 Langmuir model is shown as discontinuous dark lines, and the determined kinetic and affinity binding constants from two different RBD surfaces (see Material and methods) are given at the top of the graphs. Mean and standard deviation (SD) of five binding experiments with the indicated protein concentrations.

low compared to other Nbs/Abs analyzed in the past,[37] perhaps reflecting Nb4 recognition of a relatively inaccessible RBD site. In addition, the sensorgrams showed a slower association rate for the hcAb4 than for the Nb4. The K_D determined with the monomeric Nb4 from the kinetic rates (Figure 2c) or in ELISA binding assays (Figure S3, Wuhan) were similar and around 2 nM.

Crystal structure of the Nb4 in complex with the SARS-CoV-2 RBD

To gain insight into the Nb4 binding mode to the RBD, we determined the crystal structure of the Nb4 VHH domain

bound to the SARS-CoV-2 Wuhan RBD as described in Materials and methods. The structure was determined at 1.2 Å resolution (Table 1) and showed that the Nb bound to the outer face of the RBD and interacted with the RBM and the core (Figure 3a,b). The CC' loop of the VHH domain laid onto the RBM valley and would prevent its interaction with the N-terminal alpha-helix of ACE2, which rests on the RBM top.[53] The Nb4–RBD interface covered a large surface in the Nb4 domain and the RBD of ~1040 Å[2], which was consistent with the low kinetic dissociation rate (koff, Figure 2c). This large interface was due to the mode of the RBD recognition by the Nb4, which used the twisted β-sheet with A', G, F, C, C', and C'' β-strand (GFC β-sheet) to grasp the RBD (Figure 3a),
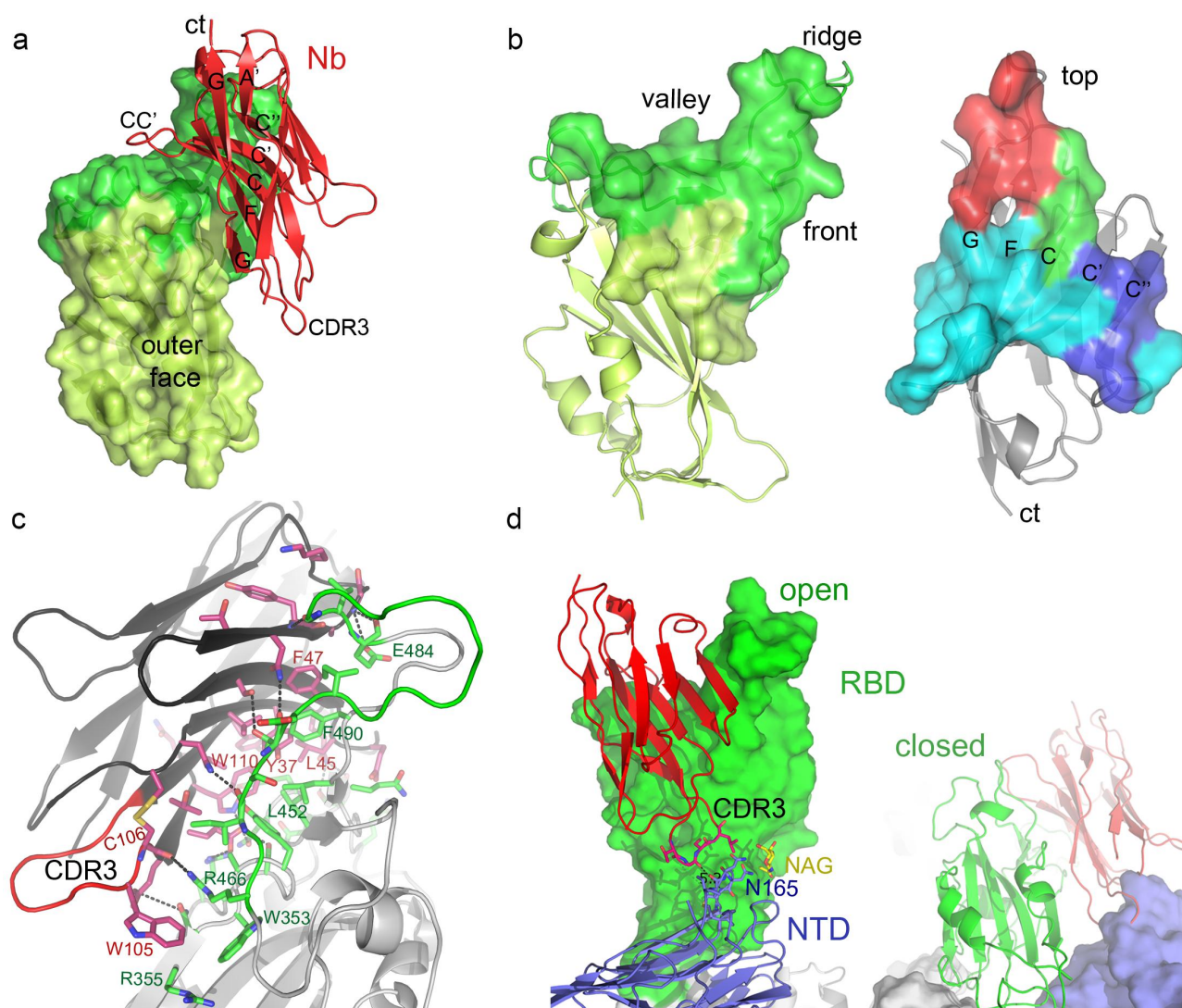
Figure 3. Crystal structure of the Nb4 bound to the RBD. (a). Ribbon and surface representations of the structure determined for the complex of the Nb4 VHH domain (red) and the SARS-CoV-2 Wuhan RBD, which is shown in green (RBM) and in light green (RBD core). The β-strands of the RBD-binding GFC β-sheet, the CDR3 and the C-terminus (ct) of the Nb4 are labeled. (b). RBD and Nb4 binding interfaces. Ribbon representations of the RBD and Nb4 (gray) with their binding surfaces in the crystal structure of the complex (determined with the PISA server). RBM and core regions in the interface are shown in green and light green, respectively, whereas the Nb4 binding region is shown with the CDR1 in green, CDR2 blue, CDR3 red and the rest of the GFC β-sheet in cyan. (c). Molecular contacts in the RBD–Nb4 binding interface. Ribbon diagrams of the RBD and the Nb4 are shown in gray and with the side chain of the residues in the interface in green and magenta, respectively. The RBD coil at the front of the domain that contacts the Nb4 is shown in green, and the Nb CDR3 in red. Key binding residues labeled and hydrogen bonds shown as dashed black lines. Oxigens in red, nitrogens in blue, and sulfurs in yellow. Interacting residues in the RBD–Nb interface are shown in Table S1. (d). Nb4 binding in the context of the S. The crystal structure of the RBD–Nb4 complex was superimposed on an open or a closed RBD of a cryo-EM structure of the SARS-CoV-2 S (PDB ID 7R4I).[37] the Nb4 domains and the S monomer with the closed RBD are shown as ribbons, while the two S monomers with the open RBD are represented as surfaces. The N-acetylglucosamine (NAG) N-linked to N165 and the NTD residues near the Nb4 CDR3 loop are shown as sticks.

including residues in and outside the complementary-determining regions (CDRs) (Figure 3b). The RBD binding interface overlapped but was distinct from class II, class III, and class V Abs (Figure S4a).[11] The binding mode of Nb4 was comparable to three previously described RBD-specific Nbs: P86, DL28, and Nb-C2–136 (Figure S4b).[29,54,55] All these Nb VHH domains lay with similar orientation on the outer face of the RBD, with the bottom of their domains on the RBM and the top toward the NTD, although the conformations of their CDR3 loops are remarkably different (Figure S4b).

The RBD–Nb4 interaction involved a complex network of nonpolar contacts in the center of the interface and polar links in the periphery (Figure 3c and Table S1). In the polypeptide that extend from R466 to E484 at the RBM edge (green in Figure 3c), several residues were engaged in hydrogen bonding with side and main chain groups of the Nb4. The RBD L452 was fully buried within the interface and its side chain pointed to a hydrophobic patch formed by the Nb4 Y37, L45, and W110 side chains. Above Y37, the Nb4 F47 in the C' β-strand stacked onto F490 in the RBD (Figure 3c). Other hydrophobic contacts included the side chain of W105 in the CDR3 of the Nb4, which approached the RBD W353 and got stuck between the side chains of R355 and R466, which was hydrogen-bonded to the carbonyl of C106 in the Nb4 CDR3 (Figure 3c and Figure S1). This is the major interaction of the Nb4 CDR3 with the RBD, which engaged the RBD front region, less accessible in the closed conformation, and engaged by class V neutralizing Abs.[10,11]

To determine Nb4 binding in the context of the S, we superimposed the RBD–Nb4 complex structure with RBDs in the open or closed conformation of a trimeric S (PDB ID 7R4I).[37] The major axes of the Nb4 VHH domain and the RBD were parallel, so the crystal structure alignment with the open RBD placed the Nb4 top, in particular the CDR3 loop, on the N-terminal domain (NTD) of the adjacent S protomer (Figure 3d). The CDR3 main chain is about 5 Å from the NTD loop that carries a glycan N-linked to N165. Flexibility in the Nb4 and NTD loops may be important for Nb binding to the open RBD in the S. Nonetheless, structural alignment of the RBD–Nb4 complex with the closed RBD in the S showed that the Nb4 CDR2 and the CDR3 collide with the NTD (Figure 3Dd), indicating that this Nb should only bind to the open RBD.

Nb4 humanization and therapeutic efficacy in K18-hACE2 mice infected with the SARS-CoV-2 Omicron BA.1

To evaluate virus neutralization *in vivo* and potential therapeutic applications of the Nb4, we first humanized Nb4 (Nb4h) by substituting specific residues in frameworks 1, 2, and 3 of the dromedary VHH domain for the most common residue in human VH3 (Table S2). By sequence comparison and alignment of Nb4 and a human VH3 consensus, we designed substitutions in Nb4 frameworks and selected a set that has been reported in humanization strategies of VHH in synthetic libraries,[56] but retained VHH hallmark residues in framework 2, corresponding to Y37, E44, L45, and F47 in Nb4. The substitutions Q1E, S11L, A14P, S49A, Q70R, K85R, and P86A were introduced into Nb4h and this humanized version was produced fused to human IgG1 Fc (hcAb4h) with similar yields to the parental clone, which suggested similar stability and folding as hcAb4. The binding capacity of the hcAb4h to the S of Omicron BA.5 was evaluated by ELISA in comparison to the parental hcAb4, which showed similar subnanomolar apparent binding affinities for both hcAbs (Figure 4a).

Next, the therapeutic potential of these hcAbs was assessed in K18-hACE2 mice. Mice were infected with the SARS-CoV-2 Omicron isolate BA.1.17, and 24 h post infection the hcAb4, hcAb4h, or a control hcAbC, which binds to a bacterial antigen, were administered via the ip route (150 μg per mouse). Then, the mice were sacrificed at 4 dpi, and the viral load in the lungs was analyzed by quantitative RT-PCR (see Materials and methods). The results showed that the administration of the hcAb4 or hcAb4h significantly reduced the SARS-CoV-2 viral load in the lungs of infected animals when compared to mice treated with the controlled hcAbC (Figure 4b). Furthermore, the hcAb4h treatment proved to be the most efficient, as 80% of the mice inoculated with humanized Ab showed a very low viral load. These data indicate a therapeutic potential for the hcAb4 and in particular for its humanized version *in vivo*.

hcAb4 neutralization of SARS-CoV-2 variants

After analyzing the therapeutic potential of hcAb4 against SARS-CoV-2 Omicron BA.1 *in vivo*, which correlated with its high-binding affinity for S or RBD, we determined the ability of the hcAb4 to prevent cell infection by several live SARS-CoV-2 virus variants following an MNT assay as described in Materials and methods. We included SARS-CoV-2 variants not previously analyzed with Nbs that have a similar RBD binding mode to Nb4,[29,54,55] and determined the hcAb4 neutralization titer (NT50) with Wuhan (D614G), Beta, Delta, BA.1, BA.5, BQ.1.1, and XBB.1.5 viruses (Figure 5a), which showed an efficient Ab neutralization of all SARS-CoV-2 variants except XBB.1.5. This demonstrated the marginal effect on the NT50 of some mutations at the Nb4 binding interface (Figure 5b), such as the E484K/A in the RBD of Beta or Omicron variants, or by the L452R substitution in the RBDs of Delta, BA.5, and BQ.1.1 viruses. Perhaps, the moderate increase in the BQ.1.1 NT50 could be due to the R346T substitution, which is also present in the XBB.1.5 subvariant that was resistant to hcAb4 neutralization (Figure 5). Nonetheless, the high NT50 determined with XBB.1.5 compared to BQ.1.1 (Figure S5) indicates that the
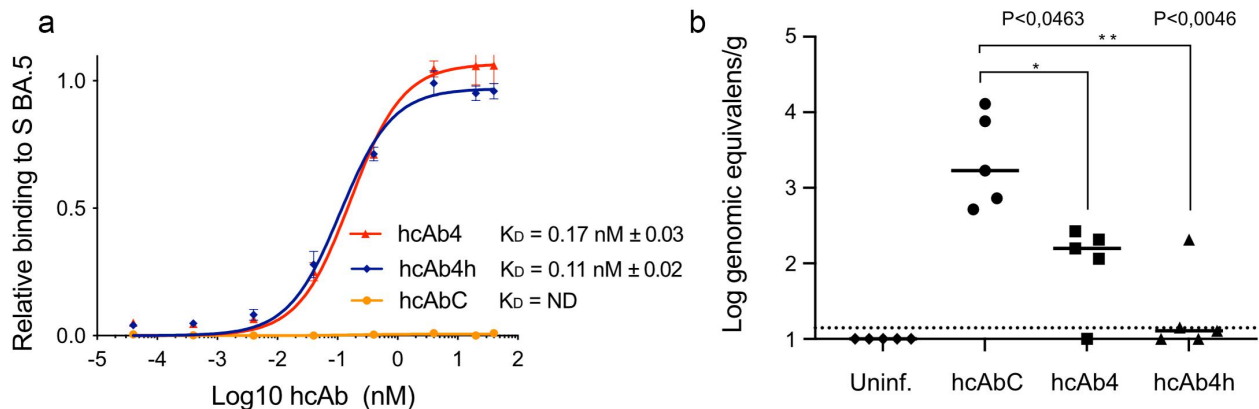

Figure 4. Nb4 humanization and therapeutic efficacy in mice infected with the SARS-CoV-2 Omicron BA.1. (a). Humanized hcAb4 binding to the SARS-CoV-2 Omicron BA.5 S. Relative binding of humanized hcAb4 (hcAb4h), native hcAb4 or a control hcAb (hcAbC) to the S protein determined by ELISA as in Figure 2a, but with 1/10 serial dilutions of the Abs. Binding K_D determined as in Figure 2a in the legend. Mean ± SEM of six independent binding assays. (b). Therapeutic efficacy of the native and humanized hcAb4 against the SARS-CoV-2 Omicron BA.1 variant. Efficacy was measured as the viral load in the lungs of K18-hACE2 transgenic mice infected with SARS-CoV-2 BA.1, determined by RT-qPCR at 4 dpi. Data from uninfected mice or infected and treated with hcAb4, hcAb4h or hcAbC 24 hours after SARS-CoV2 infection are shown. Each point represents an individual animal, and the dotted line marks the detection limit of the RT-qPCR assay. Statistically significant differences for Kruskal–Wallis test and Dunnett's correction for multiple comparisons are indicated.
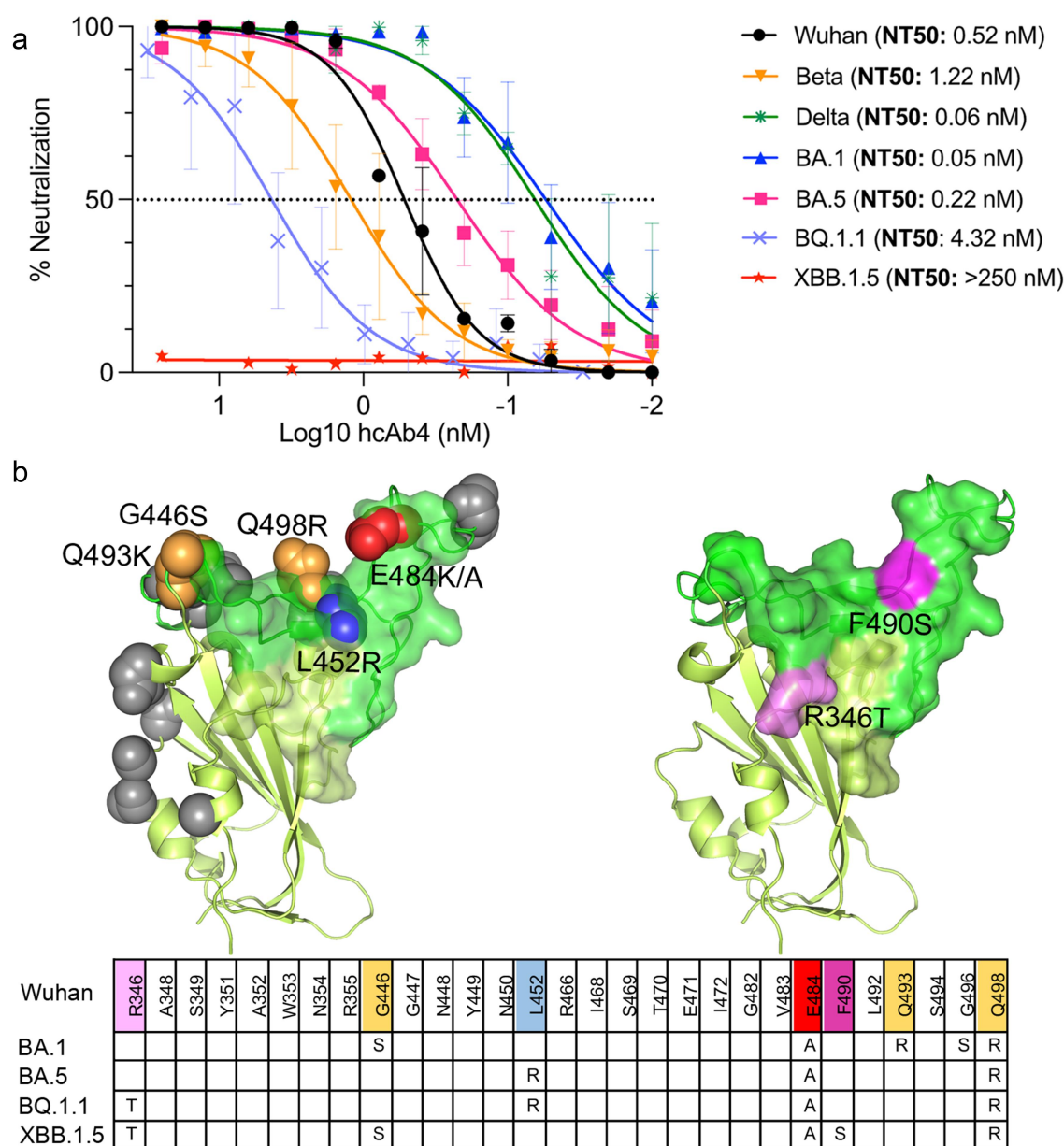
Figure 5. hcAb4 neutralization of SARS-CoV-2 variants. (a). hcAb4 inhibition of the cell infection by the indicated SARS-CoV-2 variant was determined following an MNT assay as described in Materials and methods. Neutralization was determined as the percentage of alive cells after 72 h of infection with the viruses treated with serial dilutions of the hcAb4 protein. Mean ± SEM of at least three experiments performed in triplicate were plotted, and the data were fitted to a non-linear regression model using GraphPad. Neutralization titers (NT50) were determined as the half maximal effective hcAb concentration. (b). Residue substitutions in the RBD of the Omicron variants with respect to the Wuhan strain. Left. Ribbon representation of the RBD with the Nb4 binding surface as in Figure 3b and with the side chains of the residues switched in the Omicron BA.1 or BA.5 shown with spheres. Residues outside the Nb4 binding surface are shown in gray, those in the RBD–Nb4 binding interface in orange, red or blue. Right. Additional substitutions in the XBB.1.5 RBD located in the Nb4 binding surface that may reduce hcAb4 neutralization of the subvariant. The R346T mutation is also present in the BQ.1.1 variant (pink), whereas F490S is XBB-specific (magenta). Bottom. RBD Wuhan residues in the Nb4 binding interface and substitutions in the indicated Omicron subvariants.

reduced neutralization of XBB.1.5 must be related to other RBD-specific mutations in the Nb4 binding interface with this subvariant, such as the double mutant V445P-G446S or the F490S mutation (Figure S6a), which suppresses a key contact of F490 with F47 in the Nb4 (Figure 3c) and reduces RBD and Nb4 shape complementarity (Figure S6b). We determined that among the RBD interface residues, F490 has a major contribution to the Nb4 binding energy (12.9 kcal/mol), which was calculated as described below.

Since it has been shown that Nb multimerization can overcome SARS-CoV-2 variant neutralization escape,[57] we compared the neutralization potential of the trimeric Nb4 × 3 with that of hcAb4 against the Omicron BQ.1.1, XBB.1.5, and XBB.1.16 viruses (Figure S5). The trimers improved the neutralization capacity of the hcAb4, but they only reduced about 2-fold the NT50 of the XBB subvariants with respect to the hcAb4. We found better neutralization of the XBB.1.16 than the XBB.1.5 viruses by the hcAb4 and the Nb4 × 3 proteins. In contrast, trimerization enhanced Nb4 neutralization of BQ.1.1 20-fold compared to hcAb4. These results demonstrate that a relatively high monomeric-binding activity is required for efficient SARS-CoV-2 neutralization by multimeric Nbs.

Computing RBD–Nb4 binding energies and identifying Nb4 residues with a reduced contribution to the interaction with the XBB.1.5 RBD

We used pyDock scoring function to compute the binding energy of the Nb4 residues interacting with the Wuhan RBD in the crystal structure, as well as that with the XBB.1.5 RBD modeled by two SCWRL versions (see Materials and methods). Using the SCWRL4 version for modeling, binding energy for RBD–Nb4 showed a value of −46.4 kcal/mol with the Wuhan strain and of −40.7 kcal/mol with the Omicron XBB.1.5 sub-variant. This represents a binding energy difference of +5.7 kcal/mol between XBB.1.5 and Wuhan, as expected, less favorable for XBB.1.5. Using the SCWRL3 version, the RBD–Nb4 binding energy difference between the two variants was slightly smaller (+3.5 kcal/mol).

We also computed the Nb4 residues that were most affected by the binding to the XBB.1.5 RBD compared to the Wuhan RBD. With the SCWRL4 models, these residues were F47 (+3.1 kcal/mol) and Y37 (+3.0 kcal/mol), whereas with SCWRL3, the Nb4 residues were F47 (+3.4 kcal/mol), Y37 (+3.4 kcal/mol) and G42 (+2.8 kcal/mol) (Table S3). The values for Nb4 F47 and Y37 residues were quite consistent for the two different SCWRL models, while G42 was less reliable, perhaps because this residue is in a Nb4 loop and is more solvent-exposed in the interface (Figure S6a). Thus, Nb4 residues Y37, F47, and G42 showed the highest change in their RBD binding energies when comparing the interaction of Nb4 with the XBB.1.5 RBD with respect to the Wuhan RBD (Figure 6a and Table S3). The side chains of Y37 and F47 are close to the RBD F490 (Figure 3c), which has changed to S490 in the XBB.1.5 subvariant, whereas G42 is in the Nb CC' loop that contacts the P445P-G446S double mutation in the RBD of XBB.1.5 (Figure S6a).

Generating hcAbs with high binding activity for the SARS-CoV-2 XBB.1.5 S

After identifying Nb4 residues Y37, F47, or G42 that contribute less to XBB.1.5 than to Wuhan RBD binding, we performed site saturation mutagenesis (SSM) of these residues in a construct encoding the hcAb4 followed by a screening procedure to identify mutants in the Nb4 VHH with increased binding to the XBB.1.5 RBD (Figure 6a). We mutated the Nb Y37, F47, or G42 to all possible amino acids using degenerated primers and multiple rounds of PCR as described in Materials and methods. By cell transfection, we generated a pool of hcAb mutants in cell supernatants that were screened for binding to the S of Wuhan and XBB.1.5 variants (Figure 6a). The screening yielded only two different S-binding hcAb clones with substitutions Y37F and Y37W, which showed about 10-fold higher binding for the XBB.1.5 S than the original hcAb4. No hcAb clones with increased binding activity were identified for F47 and G42 mutants. The hcAb4 mutants Y37F or Y37W showed low nM binding to the XBB.1.5 S protein, and similar apparent affinity to hcAb4 for the rest of the S variants analyzed (Figure 6b).

We then tested the hcAb4 Y37 mutants in neutralization assays with the Omicron XBB.1.5 and XBB.1.16 viruses and compared them with native hcAb4 (Figure 6c). The adapted hcAbs showed a significant increase in their neutralizing potency against XBB viruses, with NT50 values reduced by 10- to 20-fold compared to hcAb4. Nb trimerization further reduced the NT50 (Figure 6d), reaching nanomolar concentrations similar to those of hcAb4 against other variants (Figure 5). These results confirmed the validity of our approach to enhance the binding and neutralization of Nbs or Abs to the evolving SARS-CoV-2.

Discussion

The utility of vaccines and therapeutic Abs developed for SARS-CoV-2 infection can be compromised by the continuous evolution of the virus. In particular, the Omicron variant introduced numerous mutations in the S and its RBD, which reduced the neutralizing efficacy of many monoclonal Abs and the humoral immune responses induced by vaccines.[17,37,58] To overcome viral escape, several strategies have been pursued, including the identification of Omicron-specific Abs, the generation of multimeric molecules with one or more specificities, or computational approaches to restore Ab potency for new circulating variants. Here, we combined several of these approaches to generate Nb-derived molecules that showed potent neutralizing efficacy against a broad range of SARS-CoV-2 variants.

From an immune library derived from dromedaries immunized with the RBD of SARS-CoV-2 Wuhan strain, we identified the remarkably broad binder Nb4, which is specific for SARS-CoV-2 Omicron variants and even shows some interaction with the RBD of SARS-CoV-1. This suggests that the Nb4 epitope on the RBD outer face is relatively conserved among SARS-CoVs and sarbecoviruses.[24] The selection of Nb4 demonstrated the diversity of our library and the ability to find Nbs with different types of specificity by selecting the bait rather than the immunizing reagent. The binding affinity of this Nb4 for SARS-CoV-2 S was high and consistent with previous Nbs identified from the same library, confirming the stringency of the selection process[37]; the association and dissociation kinetic rates determined for Nb4 or hcAb4 binding to the RBD were low, suggesting a strong interaction to a relatively inaccessible-binding site. The tight binding (low koff, $\sim 10^{-4}$ s^{-1}) of this Nb to the RBD is consistent with the high buried surface area (~ 1040 Å^2) of the interaction revealed by the crystal structure of the RBD–Nb4 complex. In the structure, the Nb4 VHH domain grasped the RBD with its GFC β-sheet, a distinctive binding mode of antigen recognition shared by Nbs when compared to Abs,[37] which usually contact the antigen with their CDR loops and the top of their variable domains. In contrast, the Nb4 VHH domain lies along the RBD, covering its outer surface, the RBM, and the core, targeting a large epitope that is distinct from those of several classes of human Abs (Figure S4a). Most of the SARS-CoV-2 escape mutations are located in the upper half of the Nb4-binding surface, at the RBM (Figure 5b), which is engaged by the CC' loop and the C'' ridge of the Nb4 VHH domain, presumably blocking receptor recognition. On the contrary, the Nb4 epitope closer to the NTD, which makes it less accessible to Abs, is free of substitutions by SARS-CoV-2 variants
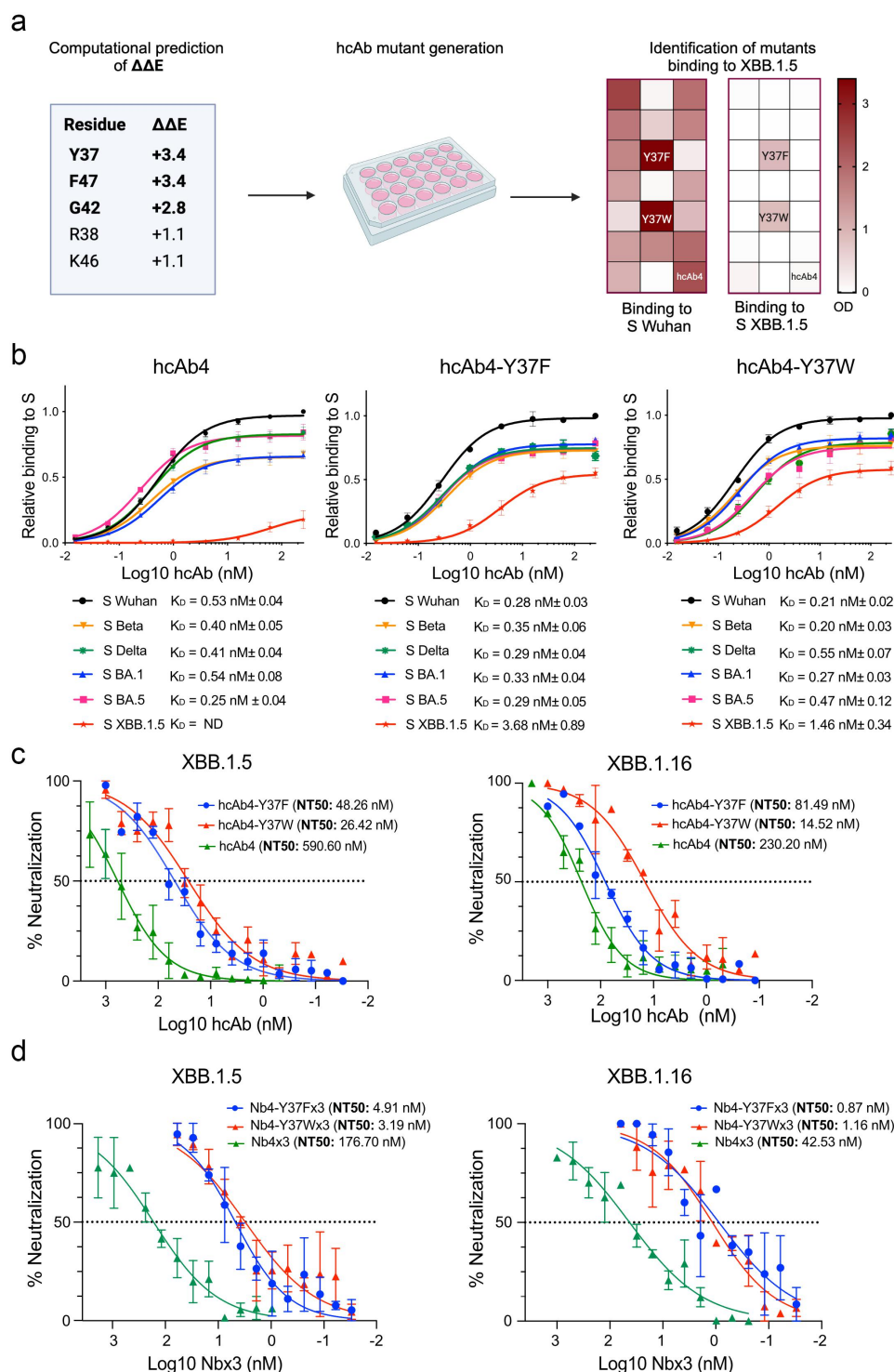
Figure 6. Adaptation of the Nb4 to the Omicron XBB.1.5 subvariant. (a). Generation of Nb4 mutants with high binding affinity for the XBB.1.5 RBD. Binding energies were calculated for Nb4 residues interacting with the Wuhan RBD in the crystal structure and a modeled XBB.1.5 RBD (see Materials and methods and Table S3); those with the largest differences in the binding energy between the variants (Y37, F47, and G42) were systematically mutated and hcAbs produced in HEK-293T cells. Supernatants containing hcAb4 mutants were used in S binding assays to Wuhan or XBB.1.5 S proteins, and the unique Y37F or Y37W with evident XBB.1.5 binding activity were identified. The plate image was generated using Biorender.com and the heatmap using GraphPad Prism version 10.2.1. (b). Binding of the native and mutant hcAb4 proteins to the S of different SARS-CoV-2 variants. Relative binding and apparent K_D were determined as in Figure 2. Mean ± SEM of four independent binding assays. (c).(d). Neutralization of the SARS-CoV-2 XBB.1.5 and XBB.1.16 viruses by native and mutant hcAb4 (c) or Nb4×3 (d) proteins. Virus neutralization in MNT assays performed with serial dilutions of the indicated proteins as in Figure 5a. Mean and SEM of three (c) or two (d) experiments performed in triplicate are plotted. The neutralization titers (NT50) determined for each protein are in the legends.

(Figure 5b). This cryptic RBD surface can be accessed by the top region of the Nb4 VHH domain and engaged its CDR3, which connected to the NTD and bound to residues at the RBD front that are hidden in the closed RBD conformation.

The high binding affinity of the hcAb4 for the S and its binding mode, which blocked RBD binding to ACE2, were likely responsible for the observed SARS-CoV-2 neutralization *in vitro* and in animal models. hcAb4 and hcAb4h

reduced SARS-CoV-2 Omicron BA.1 replication in mice when administered 24 h after infection, suggesting that the humanized Ab may have therapeutic potential against SARS-CoV-2. In addition, the hcAb4 efficiently neutralized most of the SARS-CoV-2 variants tested, with nM or sub-nM NT50 values, except for the XBB.1.5. Most of the mutations in the Omicron variants are located in the periphery of the Nb4 binding surface on the RBD (Figure 5), except for L452R, which is closer to the center of the interface, but did not significantly affect Nb4 binding to the BA.5 or BQ.1.1 sub-variants carrying this mutation. Thus, substitutions in L452 can be accommodated at the binding interface. Near the RBD L452 in the RBM (Figure 3c), the F490S mutation was probably responsible for the low hcAb4 binding activity to the XBB.1.5 S or its high NT50 for this variant. F490S abrogated the packing of the RBD F490 on the Nb4 F47 side chain and reduced the RBD–Nb4 shape complementarity (Figure S6), although it did not introduce steric hindrance. Nonetheless, SSM of F47 did not result in hcAb4 mutants with increased binding to the S observed for the Y37F or Y37W mutations. These substitutions in the Nb4 Y37 likely filled the interface cavity created by the suppression of F490 in the RBD (Figure S6), improving the Nb4 shape complementarity to the XBB.1.5. RBD and its binding affinity.

Several approaches were explored to enhance hcAb4 neutralization of the SARS-CoV-2 Omicron XBB.1.5 subvariant. The trimeric Nb4 × 3 did not significantly improve the neutralizing potency of the hcAb4, most likely due to the low affinity of the monomeric molecule. In contrast, systematic replacement of specific Nb4 residues in the binding interface resulted in hcAb4 Y37F and Y37W mutants with nanomolar binding to the Omicron XBB.1.5 S protein and improved the neutralization of the SARS-CoV-2 XBB.1.5 and XBB.1.16 subvariants by about 20-fold, which was further enhanced more than 10-fold by the trimerization of the Nb4 mutants. This strategy was based on a high-resolution structure of the RBD–Nb4 complex, but the identification of Nb4 residues with a reduced contribution to the interaction with the XBB RBD was key to expanding the neutralizing breadth of Nb4 by increasing its affinity for XBB subvariants.

Optimization of Nbs to improve binding affinity to viral variants has been attempted. Limited success was achieved for Nb adaptation to emerging SARS-CoV-2 variants by using MD simulation and docking procedures,[33] which resulted in a modest 2- to 3-fold increase in the Nb binding affinity, whereas combination of machine learning and MD gave mixed results.[32] A recently reported structure-based Nb optimization procedure using mutagenesis of Nanosota-3 residues at its RBD binding interface and phage display was able to rescue a Nb with nM binding activity to the XBB.1.5 RBD after several rounds of selection.[59] Our strategy is nonetheless more focused on key-binding contacts identified in silico, avoiding the handling of libraries and multiple screening procedures. The method used here to determine the contribution of interface residues to binding affinity has also been proven to be robust and less biased than other methods that require training of multiple parameters.[60] Note that our pyDock binding energy values (in kcal/mol) do not include explicit water contributions, configurational entropy or other energetic aspects related to conformational flexibility, so we cannot directly compare these values with the experimental binding free energies. However, the different energy terms of the pyDock scoring function, especially the accessible surface area-based desolvation potential based on atomic solvation parameters, have been optimized for protein–protein interactions, so they are appropriate to compute relative contributions of binding residues, interface hot-spot residues,[61] relative changes in energy of mutations, or alanine-scanning values.[49] The scoring function in pyDock and the server pyDockEneRes has been extensively used for the identification of energetically relevant residues and to estimate the impact of mutations on different protein–protein interactions of biomedical and biotechnological interest.[62–64] This scoring function was key here to compute binding affinities of the complex structure and modeled variants. For comparison, we also applied this method to the recently identified SARS-CoV-2 JN.1 variant using a cryo-electron microscopy (cryo-EM) structure (PDB ID 8Y5J) and determined a Nb4 binding energy to the JN.1 RBD of 2.5 kcal/mol higher than to the Wuhan RBD, suggesting a weaker binding that requires further investigation.

Once we identified the Nb4 residues that were the most affected by the XBB.1.5 mutations in the RBD–Nb4 interface, we used SSM of those residues to generate hcAb4 mutants with increased binding to the XBB.1.5 S protein, and identified only two Y37 mutations to F or W adapted to this variant. These results were consistent with the best modeled mutants for the Nb4 Y37 residue in silico, which were Y37W (−6.1 kcal/mol) and Y37F (−2.7 kcal/mol) (Table S4). No mutants of the Nb4 F47 residue with increased XBB.1.5 S binding affinity were recovered, which is also consistent with the low calculated energy of −1.1 kcal/mol for the best possible F47W mutant. So, although Nb4 F47 was close to the RBD F490 mutated to S490 in the XBB.1.5 subvariant, no substitutions in F47 substantially improved the Nb4 binding affinity for the S of XBB.1.5 in silico, and no hcAb4 mutant with increased binding was recovered. For G42, located in the CC′ loop of the Nb4 VHH domain and more exposed than Y37, no hcAb4 mutants with increased affinity were recovered, despite the modeled mutants G42W (−6.8 kcal/mol) or G42D (−3.1 kcal/mol) (Table S4). This may be due to the less reliable predictions observed for the different SCWRL versions for this residue, which may be related to the different environment of the Nb4 G42 with respect to Y37 (Figure S6). Mutations at G42 are unlikely to affect shape complementarity at the XBB RBD–Nb4 interface, as proposed above for the Y37 mutants.

The specific computational approach used here, consisting of efficient modeling of RBD variants with SCWRL based on the RBD–Nb4 complex structure, identification of the most relevant residues for escape from Nb binding with pyDockEneRes, and calculation of the impact of designed mutations on binding affinity with the pyDock scoring function, has never been used before for affinity maturation of Nbs. In addition to this computational procedure, the application of SSM and a quick screening approach resulted in the successful generation of Abs adapted to a SARS-CoV-2 variant. This strategy is easily adaptable to other Ab molecules with therapeutic potential but with a reduced affinity for specific viral variants, and it may be considered for a rapid response to emerging viruses. In addition, the research presented here

represents a successful way to generate humanized Abs with distinct binding properties and excellent virus neutralization breadth and potency, which can be applied to develop therapeutics in the course of pathogenic virus evolution.

Disclosure statement

No potential conflict of interest was reported by the author(s).

ORCID

Lidia Cerdán http://orcid.org/0000-0003-4938-5848
Daniel Rodríguez-Martín http://orcid.org/0000-0002-6838-6355
Patricia Pérez http://orcid.org/0000-0001-8983-6784
Yago Margolles http://orcid.org/0000-0003-1413-060X
Juan García-Arriaza http://orcid.org/0000-0002-5167-5724
Juan Fernández-Recio http://orcid.org/0000-0002-3986-7686
Luis A. Fernández http://orcid.org/0000-0001-5920-0638
José M. Casasnovas http://orcid.org/0000-0002-2873-6410

Ethics statement

The animal study on K18-hACE2 mice was performed in the biosafety level 3 (BSL-3) facilities at the Centro de Investigación en Sanidad Animal (CISA-INIA-CSIC) (Valdeolmos, Madrid, Spain) and was approved by the Division of Animal Protection of the Comunidad de Madrid (PROEX 115.5/21). Animal procedures were in accordance with international guidelines and Spanish law under Royal Decree (RD) 53/2013

References

1. Markov PV, Ghafari M, Beer M, Lythgoe K, Simmonds P, Stilianakis NI, Katzourakis A. The evolution of SARS-CoV-2. Nat Rev Microbiol. 2023;21(6):361–379. doi: 10.1038/s41579-023-00878-2.
2. Chen RE, Zhang X, Case JB, Winkler ES, Liu Y, VanBlargan LA, Liu J, Errico JM, Xie X, Suryadevara N, et al. Resistance of SARS-CoV-2 variants to neutralization by monoclonal and serum-derived polyclonal antibodies. Nat Med. 2021;27(4):717–726. doi: 10.1038/s41591-021-01294-w.
3. Greaney AJ, Starr TN, Gilchuk P, Zost SJ, Binshtein E, Loes AN, Hilton SK, Huddleston J, Eguia R, Crawford KHD, et al. Complete mapping of mutations to the SARS-CoV-2 spike receptor-binding domain that escape antibody recognition. Cell Host Microbe. 2021;29(1):44–57.e9. doi: 10.1016/j.chom.2020.11.007.
4. Harvey WT, Carabelli AM, Jackson B, Gupta RK, Thomson EC, Harrison EM, Ludden C, Reeve R, Rambaut A, Peacock SJ, et al. SARS-CoV-2 variants, spike mutations and immune escape. Nat Rev Microbiol. 2021;19(7):409–424. doi: 10.1038/s41579-021-00573-0.
5. Reguera J, Santiago C, Mudgal G, Ordoño D, Enjuanes L, Casasnovas JM. Structural bases of coronavirus attachment to host aminopeptidase N and Its inhibition by neutralizing antibodies. PLOS Pathogens. 2012;8(8):e1002859. doi: 10.1371/journal.ppat.1002859.
6. Piccoli L, Park Y-J, Tortorici MA, Czudnochowski N, Walls AC, Beltramello M, Silacci-Fregni C, Pinto D, Rosen LE, Bowen JE, et al. Mapping neutralizing and immunodominant sites on the SARS-CoV-2 spike receptor-binding domain by structure-guided high-resolution serology. Cell. 2020;183(4):1024–1042.e21. doi: 10.1016/j.cell.2020.09.037.
7. Barnes CO, Jette CA, Abernathy ME, Dam KMA, Esswein SR, Gristick HB, Malyutin AG, Sharaf NG, Huey-Tubman KE, Lee YE, et al. SARS-CoV-2 neutralizing antibody structures inform therapeutic strategies. Nature. 2020;588(7839):682–687. doi: 10.1038/s41586-020-2852-1.
8. Hastie Kathryn M, Li H, Bedinger D, Schendel SL, Dennison SM, Li K, Rayaprolu V, Yu X, Mann C, Zandonatti M, et al. Defining variant-resistant epitopes targeted by SARS-CoV-2 antibodies: a global consortium study. Science. 2021;374(6566):472–478. doi: 10.1126/science.abh2315.
9. Dejnirattisai W, Zhou D, Ginn HM, Duyvesteyn HME, Supasa P, Case JB, Zhao Y, Walter TS, Mentzer AJ, Liu C, et al. The antigenic anatomy of SARS-CoV-2 receptor binding domain. Cell. 2021;184(8):2183–2200.e22. doi: 10.1016/j.cell.2021.02.032.
10. Starr TN, Czudnochowski N, Liu Z, Zatta F, Park Y-J, Addetia A, Pinto D, Beltramello M, Hernandez P, Greaney AJ, et al. SARS-CoV-2 RBD antibodies that maximize breadth and resistance to escape. Nature. 2021;597(7874):97–102. doi: 10.1038/s41586-021-03807-6.
11. Jensen JL, Sankhala RS, Dussupt V, Bai H, Hajduczki A, Lal KG, Chang WC, Martinez EJ, Peterson CE, Golub ES, et al. Targeting the spike receptor binding domain class V cryptic epitope by an antibody with pan-sarbecovirus activity. J Virol. 2023;97(7):e01596–22. doi: 10.1128/jvi.01596-22.
12. Liu W, Huang Z, Xiao J, Wu Y, Xia N, Yuan Q. Evolution of the SARS-CoV-2 Omicron variants: genetic impact on viral fitness. Viruses. 2024;16(2):184. doi: 10.3390/v16020184.
13. Shrestha LB, Foster C, Rawlinson W, Tedla N, Bull RA. Evolution of the SARS-CoV-2 omicron variants BA.1 to BA.5: implications for immune escape and transmission. Rev Med Virol. 2022;32(5):e2381. doi: 10.1002/rmv.2381.
14. Yue C, Song W, Wang L, Jian F, Chen X, Gao F, Shen Z, Wang Y, Wang X, Cao Y, et al. ACE2 binding and antibody evasion in enhanced transmissibility of XBB.1.5. Lancet Infect Dis. 2023;23(3):278–280. doi: 10.1016/S1473-3099(23)00010-5.
15. Lino A, Cardoso MA, Martins-Lopes P, Gonçalves HMR. Omicron – the new SARS-CoV-2 challenge? Rev Med Virol. 2022;32(4):e2358. doi: 10.1002/rmv.2358.

16. Cao Y, Wang J, Jian F, Xiao T, Song W, Yisimayi A, Huang W, Li Q, Wang P, An R, et al. Omicron escapes the majority of existing SARS-CoV-2 neutralizing antibodies. Nature. 2022;602 (7898):657–663. doi: 10.1038/s41586-021-04385-3.

17. Arora P, Cossmann A, Schulz SR, Ramos GM, Stankov MV, Jäck H-M, Behrens GMN, Pöhlmann S, Hoffmann M. Neutralisation sensitivity of the SARS-CoV-2 XBB.1 lineage. Lancet Infect Dis. 2023;23(2):147–148. doi: 10.1016/S1473-3099(22)00831-3.

18. Wang Q, Iketani S, Li Z, Liu L, Guo Y, Huang Y, Bowen AD, Liu M, Wang M, Yu J, et al. Alarming antibody evasion properties of rising SARS-CoV-2 BQ and XBB subvariants. Cell. 2023;186 (2):279–286.e8. doi: 10.1016/j.cell.2022.12.018.

19. Lin D-Y, Gu Y, Xu Y, Wheeler B, Young H, Sunny SK, Moore Z, Zeng D. Association of primary and booster vaccination and prior infection with SARS-CoV-2 infection and severe COVID-19 outcomes. JAMA. 2022;328(14):1415–1426. doi: 10.1001/jama.2022.17876.

20. Havers FP, Pham H, Taylor CA, Whitaker M, Patel K, Anglin O, Kambhampati AK, Milucky J, Zell E, Moline HL, et al. COVID-19-Associated hospitalizations among vaccinated and unvaccinated adults 18 years or older in 13 US States, January 2021 to April 2022. JAMA Intern Med. 2022;182(10):1071–1081. doi: 10.1001/jamainternmed.2022.4299.

21. Cao Y, Jian F, Zhang Z, Yisimayi A, Hao X, Bao L, Yuan F, Yu Y, Du S, Wang J, et al. Rational identification of potent and broad sarbecovirus-neutralizing antibody cocktails from SARS convalescents. Cell Rep. 2022;41(12):111845. doi: 10.1016/j.celrep.2022.111845.

22. Liu L, Casner RG, Guo Y, Wang Q, Iketani S, Chan JFW, Yu J, Dadonaite B, Nair MS, Mohri H, et al. Antibodies targeting a quaternary site on SARS-CoV-2 spike glycoprotein prevent viral receptor engagement by conformational locking. Immunity. 2023;56(10):2442–2455.e8. doi: 10.1016/j.immuni.2023.09.003.

23. de Campos-Mata L, Trinité B, Modrego A, Tejedor Vaquero S, Pradenas E, Pons-Grífols A, Rodrigo Melero N, Carlero D, Marfil S, Santiago C, et al. A monoclonal antibody targeting a large surface of the receptor binding motif shows pan-neutralizing SARS-CoV-2 activity. Nat Commun. 2024;15 (1):1051. doi: 10.1038/s41467-024-45171-9.

24. Li M, Ren Y, Aw ZQ, Chen B, Yang Z, Lei Y, Cheng L, Liang Q, Hong J, Yang Y, et al. Broadly neutralizing and protective nanobodies against SARS-CoV-2 Omicron subvariants BA.1, BA.2, and BA.4/5 and diverse sarbecoviruses. Nat Commun. 2022;13 (1):7957. doi: 10.1038/s41467-022-35642-2.

25. Ye G, Pan R, Bu F, Zheng J, Mendoza A, Wen W, Du L, Spiller B, Wadzinski BE, Liu B, et al. Discovery of Nanosota-2, -3, and -4 as super potent and broad-spectrum therapeutic nanobody candidates against COVID-19. J Virol. 2023;97(11):e01448–23. doi: 10.1128/jvi.01448-23.

26. He L, Wu Q, Zhang Z, Chen L, Yu K, Li L, Jia Q, Wang Y, Ni J, Wang C, et al. Development of broad-spectrum nanobodies for the therapy and diagnosis of SARS-CoV-2 and its multiple variants. Mol Pharm. 2024;21(8):3866–3879. doi: 10.1021/acs.molpharmaceut.4c00165.

27. Ye G, Bu F, Saxena D, Turner-Hubbard H, Herbst M, Spiller B, Wadzinski BE, Du L, Liu B, Zheng J, et al. Discovery of Nanosota-9 as anti-Omicron nanobody therapeutic candidate. PLOS Pathogens. 2024;20(11):e1012726. doi: 10.1371/journal.ppat.1012726.

28. Chen X, Gentili M, Hacohen N, Regev A. A cell-free nanobody engineering platform rapidly generates SARS-CoV-2 neutralizing nanobodies. Nat Commun. 2021;12(1):5506. doi: 10.1038/s41467-021-25777-z.

29. Misson Mindrebo L, Liu H, Ozorowski G, Tran Q, Woehl J, Khalek I, Smith J, Barman S, Zhao F, Keating C, et al. Fully synthetic platform to rapidly generate tetravalent bispecific nanobody–based immunoglobulins. Proc Natl Acad Sci USA. 2023;120 (24):e2216612120. doi: 10.1073/pnas.2216612120.

30. Desautels TA, Arrildt KT, Zemla AT, Lau EY, Zhu F, Ricci D, Cronin S, Zost SJ, Binshtein E, Scheaffer SM, et al. Computationally restoring the potency of a clinical antibody against omicron. Nature. 2024;629(8013):878–885. doi: 10.1038/s41586-024-07385-1.

31. Longsompurana P, Rungrotmongkol T, Plongthongkum N, Wangkanont K, Wolschann P, Poo-Arporn RP. Computational design of novel nanobodies targeting the receptor binding domain of variants of concern of SARS-CoV-2. PLOS ONE. 2023;18(10): e0293263. doi: 10.1371/journal.pone.0293263.

32. Fazekas Z, Nagy-Fazekas D, Shilling-Tóth BM, Ecsédi P, Stráner P, Nyitray L, Perczel A. Evaluation of an affinity-enhanced anti-SARS-CoV2 nanobody design workflow using machine learning and molecular dynamics. J Chem Inf Model. 2024;64 (19):7626–7638. doi: 10.1021/acs.jcim.4c01023.

33. Singh V, Choudhary S, Bhutkar M, Nehul S, Ali S, Singla J, Kumar P, Tomar S. Designing and bioengineering of CDRs with higher affinity against receptor-binding domain (RBD) of SARS-CoV-2 Omicron variant. Int J Biol Macromolecules. 2025;290:138751. doi: 10.1016/j.ijbiomac.2024.138751.

34. Yang J, Lin S, Chen Z, Yang F, Guo L, Wang L, Duan Y, Zhang X, Dai Y, Yin K, et al. Development of a bispecific nanobody conjugate broadly neutralizes diverse SARS-CoV-2 variants and structural basis for its broad neutralization. PloS Pathogens. 2023;19 (11):e1011804. doi: 10.1371/journal.ppat.1011804.

35. Song T, Cooper L, Galván Achi J, Wang X, Dwivedy A, Rong L, Wang X. Polyvalent nanobody structure designed for boosting SARS-CoV-2 inhibition. J Am Chem Soc. 2024;146 (9):5894–5900. doi: 10.1021/jacs.3c11760.

36. Tong Z, Tong J, Lei W, Xie Y, Cui Y, Jia G, Li S, Zhang Z, Cheng Z, Xing X, et al. Deciphering a reliable synergistic bispecific strategy of rescuing antibodies for SARS-CoV-2 escape variants, including BA.2.86, EG.5.1, and JN.1. Cell Rep. 2024;43(6):114338. doi: 10.1016/j.celrep.2024.114338.

37. Casasnovas JM, Margolles Y, Noriega MA, Guzmán M, Arranz R, Melero R, Casanova M, Corbera JA, Jiménez-de-Oya N, Gastaminza P, et al. Nanobodies protecting from lethal SARS-CoV-2 infection target receptor binding epitopes preserved in virus variants other than omicron. Front Immunol. 2022;13:863831. doi: 10.3389/fimmu.2022.863831.

38. Casasnovas JM, Springer TA, Liu J-H, Harrison SC, Wang J-H. Crystal structure of ICAM-2 reveals a distinctive integrin recognition surface. Nature. 1997;387(6630):312–315. doi: 10.1038/387312a0.

39. Martínez-Fleta P, Alfranca A, González-Álvaro I, Casasnovas JM, Fernández-Soto D, Esteso G, Cáceres-Martell Y, Gardeta S, López-Sanz C, Prat S, et al. SARS-CoV-2 cysteine-like protease antibodies can Be detected in serum and saliva of COVID-19–seropositive individuals. The J Immunol. 2020;205(11):3130. doi: 10.4049/jimmunol.2000842.

40. McCoy AJ, Grosse-Kunstleve RW, Adams PD, Winn MD, Storoni LC, Read RJ. Phaser crystallographic software. J Appl Crystallogr. 2007;40(4):658–674. doi: 10.1107/S0021889807021206.

41. Emsley P, Cowtan K. Coot: model-building tools for molecular graphics. Acta Crystallogr D Biol Crystallogr. 2004;60 (12):2126–2132. doi: 10.1107/S0907444904019158.

42. Adams PD, Afonine PV, Bunkoczi G, Chen VB, Davis IW, Echols N, Headd JJ, Hung L-W, Kapral GJ, Grosse-Kunstleve RW, et al. PHENIX: a comprehensive python-based system for macromolecular structure solution. Acta Crystallogr Section D. 2010;66(2):213–221. doi: 10.1107/S0907444909052925.

43. Pérez P, Lázaro-Frías A, Zamora C, Sánchez-Cordón PJ, Astorgano D, Luczkowiak J, Delgado R, Casasnovas JM, Esteban M, García-Arriaza J, et al. A single dose of an MVA vaccine expressing a prefusion-stabilized SARS-CoV-2 spike protein neutralizes variants of concern and protects mice from a lethal SARS-CoV-2 infection. Front Immunol. 2022;12:824728. doi: 10.3389/fimmu.2021.824728.

44. Rodríguez-Pulido M, Calvo-Pinilla E, Polo M, Saiz J-C, Fernández-González R, Pericuesta E, Gutiérrez-Adán A,

Sobrino F, Martín-Acebes MA, Sáiz M, et al. Non-coding RNAs derived from the foot-and-mouth disease virus genome trigger broad antiviral activity against coronaviruses. Front Immunol. 2023;14:1166725. doi: 10.3389/fimmu.2023.1166725.

45. Cheng T-K, Blundell TL, Fernandez-Recio J. pyDock: electrostatics and desolvation for effective scoring of rigid-body protein–protein docking. Proteins: Struct, Function, Bioinf. 2007;68(2):503–515. doi: 10.1002/prot.21419.

46. Rosell M, Rodríguez-Lumbreras LA, Fernández-Recio J. Modeling of protein complexes and molecular assemblies with pyDock. In: Kihara D. editor. Protein structure prediction. New York (NY): Springer US; 2020. p. 175–198.

47. Canutescu AA, Shelenkov AA, Dunbrack RL Jr. A graph-theory algorithm for rapid protein side-chain prediction. Protein Sci. 2003;12(9):2001–2014. doi: 10.1110/ps.03154503.

48. Krivov GG, Shapovalov MV, Dunbrack RL Jr. Improved prediction of protein side-chain conformations with SCWRL4. Proteins: Struct, Function, Bioinf. 2009;77(4):778–795. doi: 10.1002/prot.22488.

49. Romero-Durana M, Jiménez-García B, Fernández-Recio J, Ponty Y. pyDockeneres: per-residue decomposition of protein–protein docking energy. Bioinformatics. 2020;36(7):2284–2285. doi: 10.1093/bioinformatics/btz884.

50. Bloom JD. An experimentally determined evolutionary model dramatically improves phylogenetic fit. Mol Biol Evol. 2014;31 (8):1956–1978. doi: 10.1093/molbev/msu173.

51. Starr TN, Greaney AJ, Hilton SK, Ellis D, Crawford KHD, Dingens AS, Navarro MJ, Bowen JE, Tortorici MA, Walls AC, et al. Deep mutational scanning of SARS-CoV-2 receptor binding domain reveals constraints on folding and ACE2 binding. Cell. 2020;182(5):1295–1310.e20. doi: 10.1016/j.cell.2020.08.012.

52. Salema V, Marín E, Martínez-Arteaga R, Ruano-Gallego D, Fraile S, Margolles Y, Teira X, Gutierrez C, Bodelón G, Fernández LÁ, et al. Selection of single domain antibodies from immune libraries displayed on the surface of E. coli cells with two β-domains of opposite topologies. PLOS ONE. 2013;8(9):e75126. doi: 10.1371/journal.pone.0075126.

53. Shang J, Ye G, Shi K, Wan Y, Luo C, Aihara H, Geng Q, Auerbach A, Li F. Structural basis of receptor recognition by SARS-CoV-2. Nature. 2020;581(7807):221–224. doi: 10.1038/s41586-020-2179-y.

54. Maeda R, Fujita J, Konishi Y, Kazuma Y, Yamazaki H, Anzai I, Watanabe T, Yamaguchi K, Kasai K, Nagata K, et al. A panel of nanobodies recognizing conserved hidden clefts of all SARS-CoV-2 spike variants including Omicron. Commun Biol. 2022;5 (1):1–16. doi: 10.1038/s42003-022-03630-3.

55. Li T, Zhou B, Luo Z, Lai Y, Huang S, Zhou Y, Li Y, Gautam A, Bourgeau S, Wang S, et al. Structural characterization of a neutralizing nanobody with broad activity against SARS-CoV-2 variants. Front Microbiol. 2022;13:875840. doi: 10.3389/fmicb.2022.875840.

56. Moutel S, Bery N, Bernard V, Keller L, Lemesre E, de Marco A, Ligat L, Rain J-C, Favre G, Olichon A, et al. NaLi-H1: a universal synthetic library of humanized nanobodies providing highly functional antibodies and intrabodies. eLife Sci. 2016;5:e16228. doi: 10.7554/eLife.16228.

57. Xu J, Xu K, Jung S, Conte A, Lieberman J, Muecksch F, Lorenzi JCC, Park S, Schmidt F, Wang Z, et al. Nanobodies from camelid mice and llamas neutralize SARS-CoV-2 variants. Nature. 2021;595(7866):278–282. doi: 10.1038/s41586-021-03676-z.

58. Liu L, Iketani S, Guo Y, Chan JFW, Wang M, Liu L, Luo Y, Chu H, Huang Y, Nair MS, et al. Striking antibody evasion manifested by the Omicron variant of SARS-CoV-2. Nature. 2022;602 (7898):676–681. doi: 10.1038/s41586-021-04388-0.

59. Ye G, Bu F, Pan R, Mendoza A, Yang G, Spiller B, Wadzinski BE, Du L, Perlman S, Liu B, et al. Structure-guided in vitro evolution of nanobodies targeting new viral variants. PLOS Pathogens. 2024;20 (9):e1012600. doi: 10.1371/journal.ppat.1012600.

60. Romero-Durana M, Jiménez-García B, Fernández-Recio J, Ponty Y. pyDockeneres: per-residue decomposition of protein–protein docking energy. Bioinformatics. 2019;36(7):2284–2285. doi: 10.1093/bioinformatics/btz884.

61. Grosdidier S, Fernández-Recio J. Identification of hot-spot residues in protein-protein interactions by computational docking. BMC Bioinf. 2008;9(1):447. doi: 10.1186/1471-2105-9-447.

62. Erausquin E, Glaser F, Fernandez-Recio J, López-Sagaseta J. Structural bases for the higher adherence to ACE2 conferred by the SARS-CoV-2 spike Q498Y substitution. Acta Crystallogr Section D. 2022;78(9):1156–1170. doi: 10.1107/S2059798322007677.

63. Lopez-Robles C, Scaramuzza S, Astorga-Simon EN, Ishida M, Williamson CD, Baños-Mateos S, Gil-Carton D, Romero-Durana M, Vidaurrazaga A, Fernandez-Recio J, et al. Architecture of the ESCPE-1 membrane coat. Nat Struct Mol Biol. 2023;30(7):958–969. doi: 10.1038/s41594-023-01014-7.

64. Pitsillou E, El-Osta A, Hung A, Karagiannis TC. Epimaps of the SARS-CoV-2 receptor-binding domain mutational landscape: insights into protein stability, epitope prediction, and antibody binding. Biomolecules. 2025;15(2):301. doi: 10.3390/biom15020301.